

NUMERICAL MODELLING OF THE THERMO-MECHANICAL RESPONSE OF A ROCKET MOTOR TO EXHAUST GASES LOAD

MAŁGORZATA ORŁOWSKA

Military University of Technology, Faculty of Mechatronics and Aerospace, Warsaw, Poland

ANDRZEJ J. PANAS

*Military University of Technology, Faculty of Mechatronics and Aerospace, Warsaw, Poland and
Air Force Institute of Technology, Warsaw, Poland*

KAROL REĆKO

Military University of Technology, Faculty of Mechatronics and Aerospace, Warsaw, Poland

ANDRZEJ ŻYLUK

Air Force Institute of Technology, Warsaw, Poland; e-mail: andrzej.zyluk@itwl.pl

A numerical model for analysis of thermal and mechanical loads of a rocket motor has been developed. This model of a solid propellant motor corresponds to a short range, fast launch and cruise type missile. It has been elaborated using the Finite Element Method (FEM) incorporated into commercial Comsol/M code. The experimental data on the thrust profile have been utilised to develop proper initial and boundary conditions for forgoing numerical calculations. The studies have been focused on the temperature and stress evolution within the case and nozzle section of the rocket engine. A special attention has been paid to the graphite insert of the rocket motor throat. The performed analyses proved effectiveness of the modelling methodology that will be applied to investigations of the modified motor performance.

Keywords: solid propellant rocket motors, thermo-elastic FEM analysis, nozzle thermal load

1. Introduction

Despite a relatively simple design (Mattingly and Ohain, 2006; Oates, 1997; Sutton and Biblarz, 2001), a rocket motor creates a challenging task in precise analysis of its working parameters and characteristics. It is because of ultra high temperature and high pressure of the exhaust gases acting on the construction at the working cycle. This is the case when a short range – short operation time missiles are taken into consideration. For these reasons, problems of the short range solid state rocket motor design optimisation still attracts attention of the research community in many aspects. A variety of recent works account for design optimisation, high frequency solid propellant combustion instability (Safta *et al.*, 2011), initial stage exhaust gases temperature decrease (Żyluk and Pietraszek, 2014) *etc.* Preiskorn *et al.* (2011) carried out numerical investigation of motor nozzle thermal loads while Morozov and Pitot de la Beaujardiere (2009) investigated thermostructural interaction of a composite rocket case. In both of the above mentioned papers, the authors underlined the fact that the literature on the thermal and mechanical shock of the rocket motor components is relatively scarce.

The purpose of this work was to perform numerical analysis of coupled thermal and mechanical loads of the short range missile rocket motor (Grabowska, 2012). The analysis was based on experimental data of the exhaust gases pressure and temperature time histories. Developing the numerical model, the temperature dependence of material properties was accounted for. Some of the thermophysical properties were obtained in the course of the appropriate measurements.

Two numerical packages were used for numerical simulation: main calculations were performed applying Comsol Multiphysics FEM (Finite Element Method) software while auxiliary studies were conducted employing Ansys code. Prior to the main calculations, all numerical procedures had been validated in the course of additional studies. Next, dynamic thermostructural studies were conducted. Finally, the results of studies were analysed and the operational response of the nozzle motor rocket section was evaluated in various aspects.

2. The processes modelling

The objective in developing the model for combined thermo-static calculations was to create a structure that exhibits the general features common to the most solid propellant rocket motor designs and allows for analysis of the main high temperature processes and their effects. Amongst them, effects of thermal and mechanical loads of the combustion chamber casing and thermal load of the nozzle throat structure should be reliably reflected. Moreover, the methodology of the proposed numerical simulation should be universal and easy to accommodate to any other case study. This is important in view of any possible modifications of the analysed construction like those described in Morozov and Pitot de la Beaujardiere (2009). On the other hand, the model should possess sufficient simplicity to allow for focusing on certain aspects of its behaviour.

In the present case, the stressed effects were: the effect of heat withdrawal from the nozzle throttle and the effect of structure resistance to thermo-mechanical load from the combustion gases flow. As it can be seen, physics of the investigated phenomena includes propellant combustion, exhaust gases supersonic flow, heat transfer from gases to the rocket motor internal walls, exhaust gases pressure load, heat conduction within the motor structure, thermo-mechanical coupling within the object structure and, finally, combined convective-radiative heat withdrawal at outer object surfaces. What makes the study more difficult is that the processes should be analysed in their transients. In order to simplify the problem, the analysis was divided into several subsequent stages of combined analytical-numerical calculations. The simulation points included two phases of numerical modelling which were: numerical modelling of a stationary supersonic flow within the rocket nozzle and numerical modelling of the combined transient heat transfer and static thermo-mechanical load of the motor rocket structure. The results of exhaust gases flow modelling were applied to complement the outcome of 1D analytical modelling of the flow – these results were incorporated into boundary conditions for the main numerical calculations of heat transfer and stress evolution within the motor structure. Developing the structure model, a special attention was put on a proper definition of the material properties. The definitions reflected both the temperature and directional dependence of them. Last but not least, the definitions were applied in such a way that the ablation effects could have been easily included into the analysis.

2.1. The overall rocket motor model and material properties

The geometrical model was based on a certain construction of a short range missile solid propellant rocket motor (Grabowska, 2012). For the purpose of numerical analysis, the real design was simplified to 2D axial symmetric geometry that is shown in Fig. 1. As it can be seen, only the ending part i.e. nozzle section was modelled. It is because only this part, of the rocket motor is exposed to high pressure, high temperature exhaust gas flow. Basic dimensions of the object are: the nozzle throat of 14.5 mm diameter, the maximum diameter of the object equal to 64 mm and the total object length along the Oz coordinate equal to 120 mm. Developing the geometry of the model several subdomains were defined for the purpose of the following parametric meshing facilitation. The individual subdomains are composed of three main structural domains that correspond to three constructional materials: pyrolytic graphite, graphite and constructional

steel (see Fig. 1). The nozzle throat is made of pyrolytic graphite. This material is not only temperature resistant but is characterized by orthotropic thermal and mechanical properties. In the described configuration, it exhibits high radial thermal conductivity that exceeds axial thermal conductivity by two orders of magnitude. This facilitates heat removal from the inner throat surface and prevents the nearby nozzle sections from conductive heating. The divergent part of the motor nozzle is made of thermally resistant POCO graphite. The basic structure of the rocket motor is made of constructional steel.

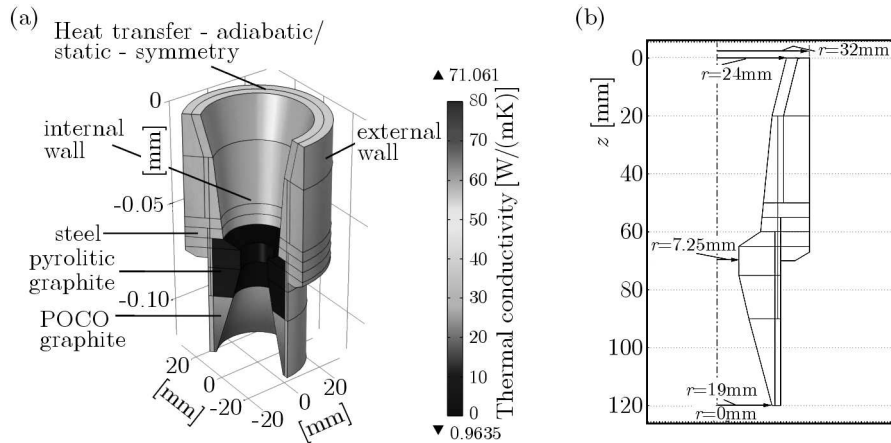


Fig. 1. The analysed axisymmetric rocket nozzle structural architecture in 3D projection (a) and in 2D cross-sectional view (b). The orthotropic pyrolytic graphite, isotropic POCO graphite and isotropic steel sections are indicated by values of thermal conductivity in the axial, i.e. Oz direction

Regarding the expected high temperature structure loading, the material properties of the three substructures were defined temperature dependent. In addition, the pyrolytic graphite was assumed to be orthotropic. The basic data on thermal and mechanical properties were taken according to Material Property Database MPDG v.7.08 (2009) and Preiskorn *et al.* (2011), but certain figures concerning pyrolytic graphite thermal conductivity and heat capacity were supplemented by results of our own studies (see e.g. Panas (2011)). For the simulation, the material properties temperature dependencies were described by appropriate analytical expressions in Comsol software syntax (Grabowska, 2012) and then were incorporated into subdefinitions of the model properties. A complete description of the applied model data is provided both in Table 1 and Figs. 2-4. The figures illustrate the thermophysical property (TP) temperature changes by showing a certain property as the ratio to its room temperature (RT) value. The RT values were taken at 20°C .

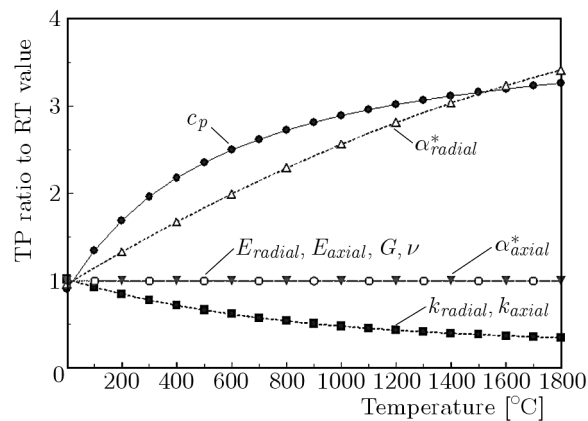


Fig. 2. Temperature dependencies of thermophysical properties of pyrolytic graphite (nozzle throat)

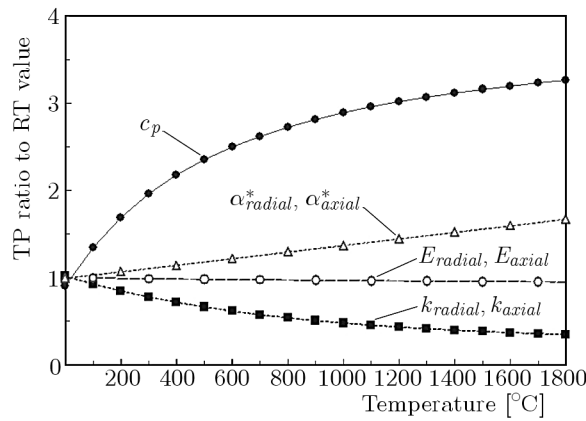


Fig. 3. Temperature dependencies of thermophysical properties of POCO graphite

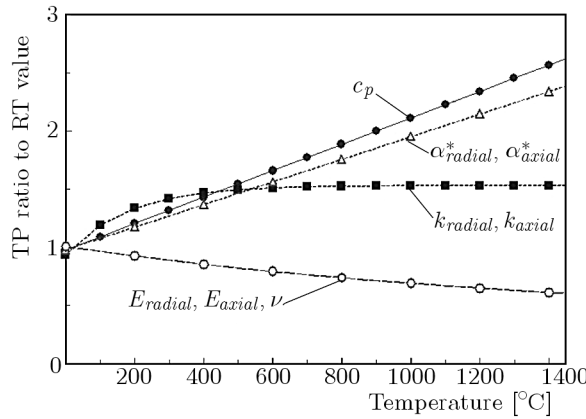


Fig. 4. Temperature dependencies of thermophysical properties of constructional steel – the main structural rocket motor material

Table 1. Room temperature (20°C) values of the assumed thermal and mechanical material properties (comp. also Figs. 2, 3 and 4)

Property	Direction	Pyrolytic graphite (orthotropic)	POCO graphite (isotropic)	Steel (isotropic)
Density ρ [kg m ³]	n.a.	2200	1670	7670
Thermal conductivity k [W/(mK)]	radial	250	97.5	17.3
	axial	2		
Thermal expansivity (CTLE* ¹) α^* [$10^{-6}/K$]	radial	1.64	6.90	10.9
	axial	27		
Heat capacity c_p [J/(kg K)]	n.a.	683	683	482
Young's modulus E [GPa]	radial	4.8	14.2	208
	axial	0.48		
Shear modulus G_{rz} [GPa]	n.a.	1.6	n.a.	n.a.
Poisson's ratio ν	radial	0.30	0.30	0.32
	axial	0.30		

¹ Coefficient of the thermal linear expansion

The model was meshed applying quadrilateral elements as it is shown in Fig. 5. This mesh was used both in transient thermal and in static structural calculations. For the purpose of visualisation of the resultant data, seven control points were defined: two placed close to the surface of the internal wall of the combustion chamber, three located at the critical region of the nozzle throat, one placed at the divergent part of the nozzle and one at the outer surface of the rocket motor structure. It is worth to mention that some of the subdomain border lines were assigned to accommodate thermal contact resistance. It concerns e.g. the border between the pyrolytic graphite and steel elements. This was a step towards further model improvements but in the presently discussed case this particular phenomenon was discarded from considerations.

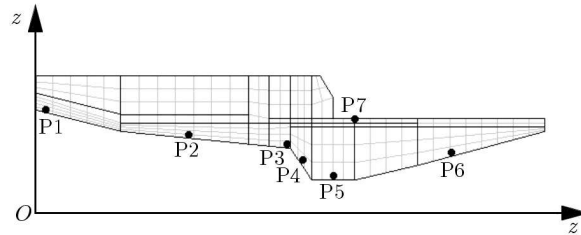


Fig. 5. The model meshing and indication of the control points for the resultant data collection

2.2. Boundary conditions

The thermal and pressure loading data applied to the analysis were taken according to certain experimental data (Grabowska, 2012) of the rocket motor investigation. In the course of these studies, several test firings were performed. From the combustion chamber internal temperature and pressure measurements, the model nozzle inlet conditions were accepted to be equal to 10 MPa and 3500 K during the first stage of motor operation and 3 MPa and 3500 K during the second stage. Duration of the first stage was equal to 3 s, the next one lasted 6 s, which gave 9 s of the motor running in total.

In order to define the nozzle wall pressure distribution and other boundary conditions, the auxiliary stationary flow calculations were conducted first. The Computer Fluid Dynamics (CFD) Ansys Fluent software was utilised to develop the axisymmetric model of the nozzle of the geometry corresponding to that shown in Fig. 1. The structural mesh was defined and two sets of the appropriate inlet and outlet conditions were established which reflect the above described stagnation conditions of the two stage rocket operation. For the nozzle flow calculation, an isentropic flow of an ideal gas of air properties was assumed. However, the gas parameters were taken temperature dependent applying standard Ansys Fluent software functions. The calculations were conducted within the frame of the $k-\epsilon$ turbulence model. An example of preliminary results of CFD calculations is shown in Fig. 6. The raw simulation data were processed afterwards to obtain distributions of flow parameters along the symmetry line. The results are shown in Fig. 7. As it can be seen, a distinct difference between the 10 MPa and 3 MPa inlet pressure cases was revealed only in the instance of pressure distribution. The appropriate temperature and velocity curves overlap each other.

Purposely to confirm the CFD outcome, these results were confronted with the results of analytical calculations. For this particular analysis, a 1D isentropic ideal gas flow was assumed. The gas thermodynamic properties were taken as for the air. Applying standard formulae (comp. e.g. Oates, 1997; Torecki, 1984; Mattingly and Ohain, 2006), the study results were achieved that agree with the CFD ones for about few percent (Grabowska, 2012). This confirmed reliability of the CFD data which were utilised to define model boundary conditions (BC) applied to the internal structure wall (comp. Fig. 1). The pressure and temperature loads were represented by piecewise linear functions as it is shown in Fig. 8 – each function mimics the appropriate CFD

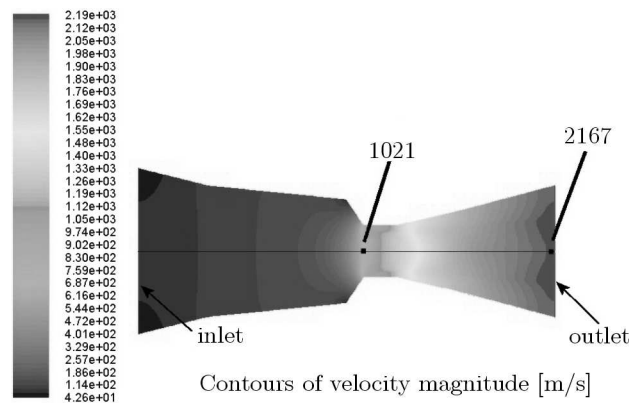


Fig. 6. Example of the auxiliary CFD simulation results – stationary velocity field distribution for the inlet stagnation gas pressure equal to 10 MPa, inlet stagnation temperature equal to 3500 K and the open boundary outlet pressure 0.1 MPa. The label scale covers the interval from 43.6 m/s to 2190 m/s

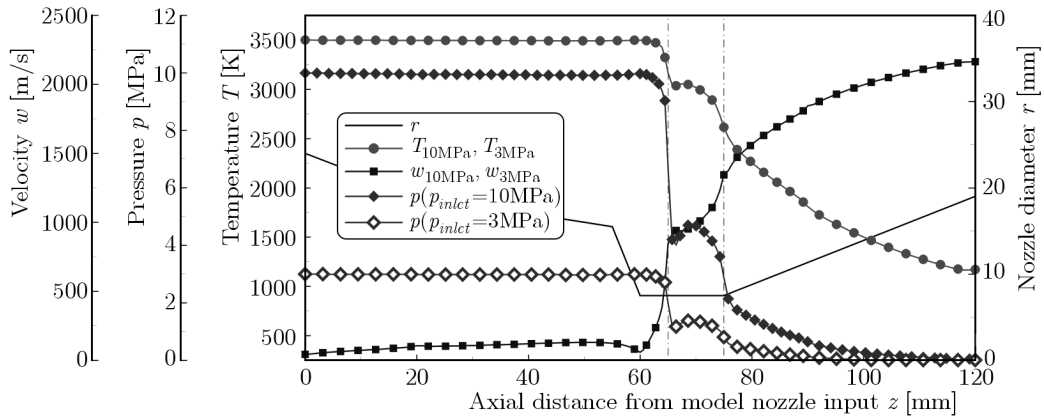


Fig. 7. Axial distribution of the nozzle flow velocity, pressure and temperature from CFD simulations – the nozzle throttle is indicated by vertical dashed lines

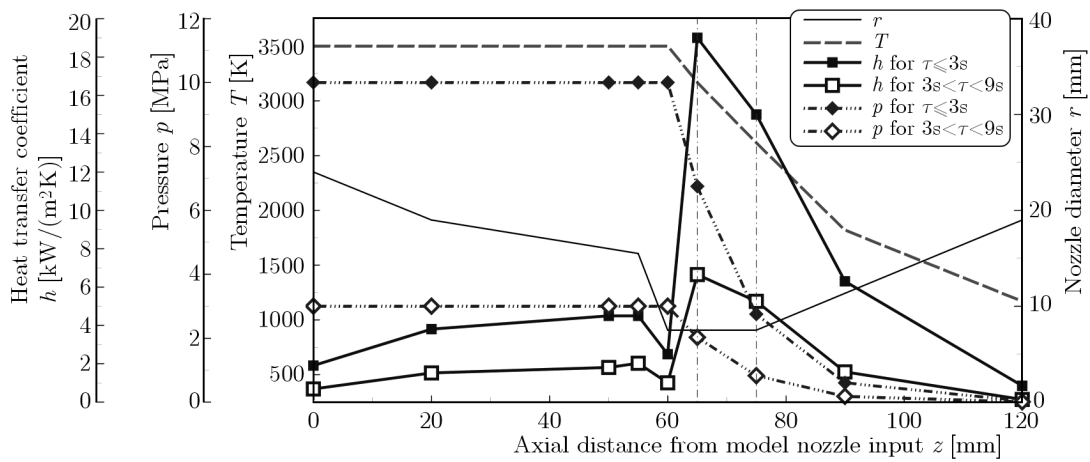


Fig. 8. Assumed axial distributions of the BC temperature, pressure and heat transfer coefficient – the nozzle throttle is indicated by vertical dashed lines

result. In order to define the last one BC parameter, i.e. the heat transfer coefficient h , the following Adams criterion formula was employed (Preiskorn *et al.*, 2011)¹

$$\text{Nu} = 0.026\text{Re}^{0.8}\text{Pr}^{0.4} \quad (2.1)$$

The Nusselt, Reynolds and Prandtl similarity numbers were defined as

$$\text{Nu} = \frac{h(z)2r(z)}{k_g[T(z)]} \quad \text{Re} = \frac{w(z)2r(z)}{\nu_g[T(z)]} \quad \text{Pr} \equiv 0.7 \quad (2.2)$$

where w is the local flow velocity, r is the nozzle channel local radius and k_g is the gas thermal conductivity (Wiśniewski, 1972)

$$k_g = 2.442 \cdot 10^{-4}T^{0.82} \quad (2.3)$$

The kinematic viscosity ν_g is derived from the gas actual density ρ_g and the modified dynamic viscosity μ_g through Sutherlands formula (Wiśniewski and Wiśniewski, 2000) in the following manner

$$\nu_g = \frac{\mu_g}{\rho_g} = \frac{\mu_g}{p}RT \quad (2.4)$$

where

$$\mu_g(T) = 17.3 \cdot 10^{-6} \left(\frac{T}{273.15} \right)^{0.62} \quad R = 287 \frac{\text{J}}{\text{kg K}} \quad (2.5)$$

The heat transfer coefficient distribution in the two discussed pressure load cases, i.e. the initial rocket firing stage 10 MPa and the next 3 MPa stage, is illustrated in Fig. 8. It should be underlined that these particular boundary conditions were applied to the internal structure boundary (comp. Fig. 1). As it concerns the outside boundary, several Nu criteria formulae for the external flow were taken into account. In that range the Bejan (Bejan and Kraus, 2003) and Zhukauskas (Wiśniewski and Wiśniewski, 2000) models for the cross flow over cylinder, the standard model for flow over the plate (Bejan and Kraus, 2003; Wiśniewski and Wiśniewski, 2000), and the Stchitnikov model (Madejski, 1998) for the axial flow over a cylinder were applied. After several analyses, applying the rocket technical data (Grabowska, 2012), several figures for the heat transfer coefficient were obtained ranging from 110 W/(m²K) to 730 W/(m²K). Eventually, it was decided to assume the external heat transfer coefficient 400 W/(m²K) and the fluid temperature equal to 273.15 K. In addition, the radiative heat losses were added to the model by assuming the external wall emissivity $\varepsilon = 0.7$, and the ambient temperature also equal to 273.15 K. The same BC were applied to the annular base at the divergent part of the nozzle ($z = 12$ mm). As it concerns the annular “upper” surface ($z = 0$ mm), this boundary was assumed to be symmetric. It results in the adiabatic condition for heat transfer, while the structural constraints were defined as radial rolling and axial fixing. One can notice that the dynamical load due to the rocket acceleration onto the wall structure had been excluded from considerations but it not contributes much to the considered phenomena. The same concerns the previously discussed external convective heat losses. It is because a relatively short period of the rocket motor operation was combined with a relatively high structure heat capacity.

¹Developing the model, alternative Davey’s formulae (comp. e.g., Wiśniewski, 1972; Davey, 1963) have been considered also. However, the appropriate test resulted in more than twice lower h values in comparison with the Adams formula. In order to avoid underestimation of the structure loads, it was decided to apply the last one.

2.3. The solution procedure

The rocket motor nozzle structure was subjected to thermal and mechanical load, and the transient response of the system was observed. To develop a solution to the thermostructural problem, the Comsol code utilises a two stage solution scheme that results in an uncoupled thermostructural result. At the first stage, the heat transfer problem was analysed. This part allows transient analyses to be performed that terminate in the temperature distribution in the object as function of time. The static structural solver uses it to determine the thermal strain generated by thermal excitation and combines this loading with the assumed mechanical one. Utilising the temperature distribution, the material properties were simultaneously modified according to appropriate definitions. As it can be seen, the final thermostructural solution is uncoupled: the thermal field has an effect on the stress and strain fields but not contrariwise.

In our case a transient analysis was performed that covered the time interval of 12 s in total: 3 s of the initial action phase, 6 s of the second stage and 3 s of an arbitrarily assumed final system relaxation time. At the time equal to 3 s, the appropriate pressure loading and the heat transfer coefficient distribution (comp. Fig. 8) were switched from the case corresponding to 10 MPa to the case of 3 MPa stagnation conditions. For the last stage, the convective heat transfer on the internal wall was “turned off”, which means that the adiabatic boundary condition was adopted. The analysis was performed at a 0.1 s time step. The same was the rate of the solution sampling.

3. Results and discussion

For the purpose of detailed identification of thermostructural effects inside the considered rocket motor nozzle, transient thermal and quasi-static structural analyses were carried out. One of the expected results was confirmation that the nozzle would operate within a reasonable thermal and structural envelope. The rocket motor structure was subjected to distributed thermal and structural loads that were changed twice: at 3 s of operation and at 9 s of operation, as was described in the previous chapter. These main calculations were supplemented by auxiliary ones performed to follow the effects of alteration of the inside and outside convective heat transfer condition on the final results. In these particular analyses, the effect of the outside wall heat transfer coefficient changes from 400 W/(m²K) to 110 W/(m²K) and the effect of the Adams model replacement by Davey’s one (comp. Section 2.2) on the maximum temperature of the inside wall were tested.

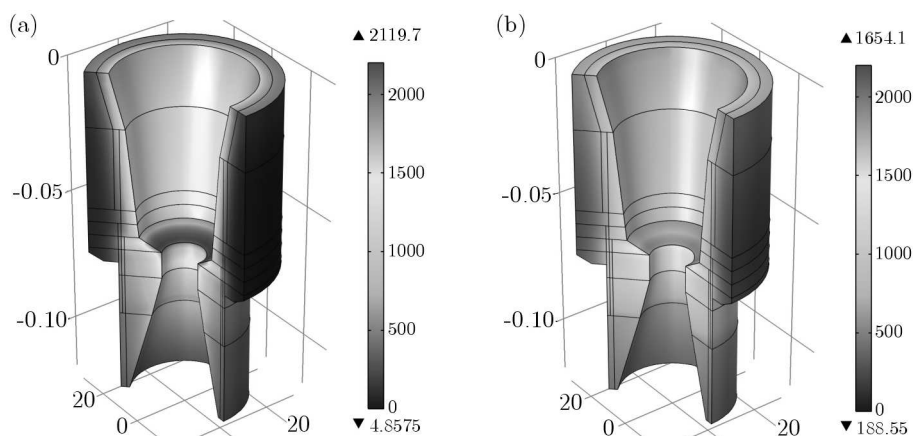


Fig. 9. Comparison of the temperature distribution for time instants: $\tau = 3$ s (a) (maximum temperature 2119.7°C) and $\tau = 9$ s (b) (maximum temperature 1654.1°C); the gray legend covers the interval from 0 to 2200°C

As it is shown in Fig. 9, the maximum values of temperature occur, as was expected, inside the rocket motor structure. The temperature evolutions at control points are displayed in Fig. 10. As it can be easily observed, the displayed time histories followed the assumed BC changes at 3 s and at 9 s of the motor operation. The whole structure experienced the maximum temperature load at 1200°C. The maximum temperature equal to 2119.7°C was recorded at the convergent section of the pyrolytic graphite insert. The steel made structure experienced the maximum internal temperature equal to about 1200°C. Such a temperature was revealed at the border line of the convergent steel section nearby its center regarding to the axial direction. The temperature of 1200°C is dangerously close to the material property limits, especially regarding the strength decrease with the increasing temperature (Material Property Database MPDG v.7.08, 2009), but it occurred only within the thin skin layer of the internal wall. In reality, the structure is additionally protected by ablation effects (comp. eg. Sutton and Biblarz (2001) or Torecki (1984)), but this particular phenomenon has not been considered developing the present model. However, the simulation results confirm proper functioning of the orthotropic pyrolytic graphite insert that is shown in Fig. 11. Despite the fact that the adjacent nozzle throat section experienced maximum temperature rise, the steel structure was exposed at the point P3 only to about 1100°C. The same conclusion can be drawn from the analysis of time evolution curves of the total heat flux at the control points, which is displayed in Fig. 12. Heat fluxes at P4 and P5 are greater for more than three times than those registered elsewhere, and this phenomenon can undoubtedly be attributed to specific properties of pyrolytic graphite.

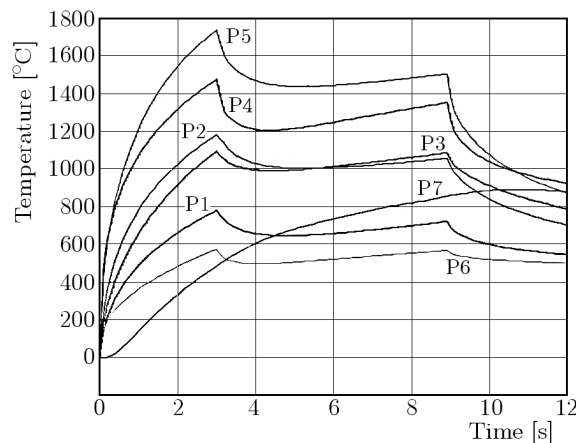


Fig. 10. Temperature changes at the defined control points (comp. Fig. 2) during rocket motor operation ($0\text{ s} \leq \tau \leq 9\text{ s}$) and at relaxation ($9\text{ s} < \tau \leq 12\text{ s}$)

It is interesting to confront the above discussed results to the results of auxiliary calculations. Application of Dayve's model for the heat transfer coefficient at the inner wall resulted in a substantial decrease in the temperature rise. The maximum temperature recorded was equal to 1822.7°C, that is about 300°C lower than that obtained for the Adams model, Eq. (2.1). It confirms the model sensitivity to the internal flow parameters. On the contrary, about four times lower values of the outside heat transfer coefficient resulted in negligibly small maximum temperature changes for the operational time interval ($\tau \in [0\text{ s}, 9\text{ s}]$). The changes at $\tau = 3\text{ s}$ were of about 1 deg. However, the final maximum temperature recorded within the investigated structure was equal to about 1190°C, that is about 140°C greater than that derived in the main calculations.

The maximum values of stress occurred also at 3 s of motor operation at the internal boundary of the steel made construction part. The appropriate von Mises stress value distribution is shown in Fig. 13a, while the stress evolutions in time are displayed in Fig. 13b. As in the case of thermal results, the time histories followed the assumed BC changes. In total, the observed

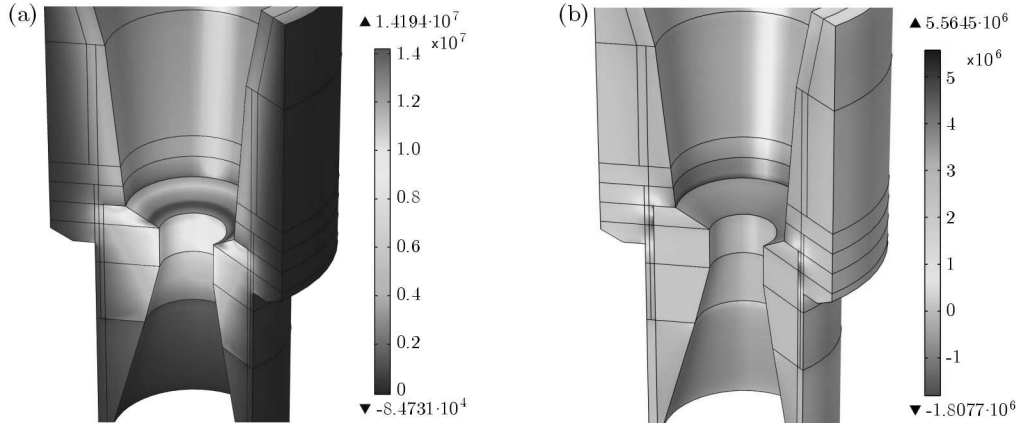


Fig. 11. Radial (a) and axial (b) heat flux mapping in W/m^2 at $\tau = 4$ s shows typical behaviour of the pyrolytic graphite nozzle throat insert that radially removes heat from the inside and blocks the axial heat conduction from the most exposed to thermal load region of the nozzle to the steel structure

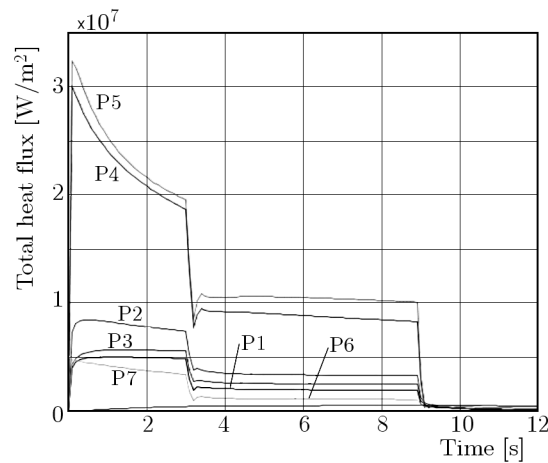


Fig. 12. Total heat flux changes recorded at the control points (comp. Fig. 2)

values do not exceed the material strength despite the fact that this particular property decreases with the temperature increase (comp. e.g. Material Property Database MPDG v.7.08, 2009). Commenting on the strain-displacement results (comp. Figs. 14a and 14b) it should be noted that maximum values did not follow the BC changes as it was observed in the previous cases. For instance, the maximum radial displacement of the internal part of the structure occurred at the end of the thermal excitation, i.e. at $\tau = 9$ s. The lag in time of the extremum occurrence was increasing while the radial distance was being magnified. The phenomenon can be undoubtedly attributed to heat accumulation within the structure.

In general, the observed thermal and structural values confirm that the whole structure would operate within a reasonable thermal and structural envelope. However, this concerns only the assumed motor operation time. Any possible extension of the operation time or an increase in thermal load parameters requires modifications to be introduced into the developed model. In particular, the ablation effects should be accounted for. However, the developed model design is open for such changes and the appropriate alterations can be easily incorporated into the material property definitions. While planning any other future studies, it is worth to suggest an extension of the analysis into the dynamic structural response. Though, such a study needs the load conditions to be redefined.

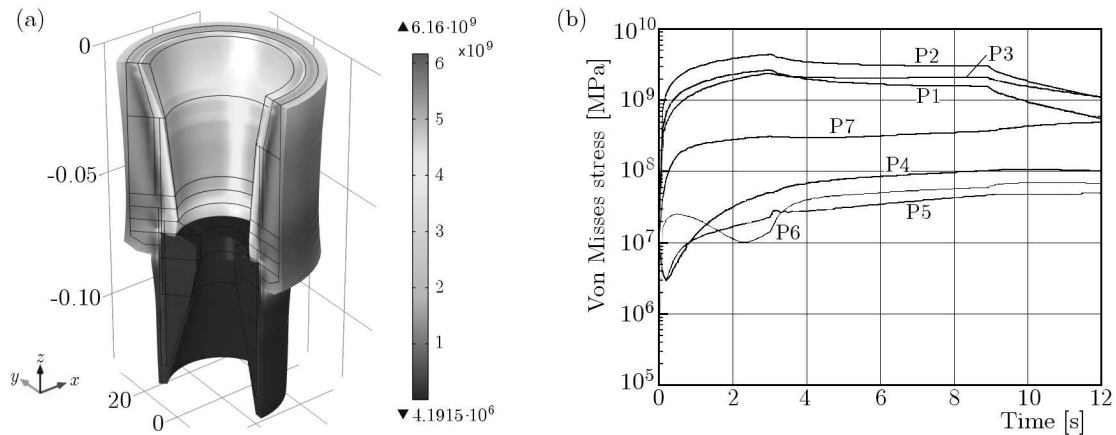


Fig. 13. Von Mises stress in Pa at $\tau = 3$ s, (a) object deformation illustrating the displacement field, (b) changes of the von Mises stress values recorded at the control points in the logarithmic scale

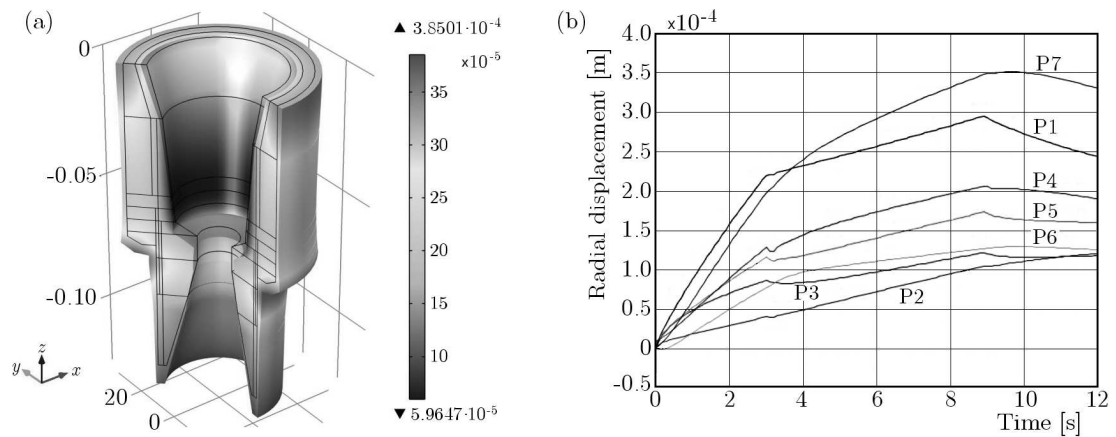


Fig. 14. The radial displacement of the structure in m at $\tau = 9$ s, (a) object deformation illustrating the displacement field, (b) radial displacement evolution recorded at the control points

4. Conclusions

The present study shows the thermostructural response of a solid propellant rocket motor response. The analysis was carried out by numerical simulation. In order to perform the appropriate investigations, a relevant numerical model was developed. Applying the solid propellant motor firing data, the appropriate boundary conditions were defined and incorporated into the developed model. The numerical model accounts for both thermal and mechanical loads. This distinguishes it from the model presented by Preiskorn *et al.* (2011). Accounting for the temperature changes in the material properties makes it different from the similar design analysed by Oates (1997). The performed calculations proved feasibility of the sophisticated parametric structure of the developed model and confirmed correctness of the applied methodology of the studies. Moreover, the analysis of the obtained results made it possible to establish the needs for the most needed alterations. In the nearest future, the developed methodology will be utilised to analyse more advanced designs.

References

1. BEJAN A., KRAUS A.D., 2003, *Heat Transfer Handbook*, John Wiley & Sons, Inc., New York
2. DAVEY T.B., 1963, Entrance region heat transfer coefficients, [In:] *Heat Transfer*, vol. 59, American Institute of Chemical Engineers; 1st Edition, 37-45

3. GRABOWSKA M., 2012, Analysis of thermal load of a nozzle of short range missile rocket motor, MSc Thesis, Military University of Technology, Warsaw
4. MADEJSKI J., 1998, *Heat Transfer Theory*, Wydawnictwo Uczelniane Politechniki Szczecińskiej, Szczecin, pp. 266
5. Material Property Database MPDG v.7.08, 2009, JAHM Software, Inc., USA
6. MATTINGLY J.D., OHAIN H., 2006, *Elements of Propulsion: Gas Turbines and Rockets*, AIAA Education Series, The American Institute of Aeronautics and Astronautics, Inc., Reston, Virginia
7. MOROZOV E.V., PITOT DE LA BEAUJARDIERE J.F.P., 2009, Numerical simulation of the dynamic thermostructural response of a composite rocket nozzle throat, *Composite Structures*, **91**, 412-420
8. OATES G.C., 1997, *Aerothermodynamics of Gas Turbine and Rocket Propulsion*, AIAA, Inc., Reston, Virginia
9. PANAS A.J., 2011, IR support of thermophysical property investigation. Medical and advanced technology materials study, [Chapter 4 in:] *Infrared Thermography*, Raghu V. Prakash (Edit.), Intech, 2011, 65-90
10. PREISKORN M., KONIORCZYK P., ZYGMUNT B., 2011, Numerical calculations of non-stationary temperature fields in non-cooled short-range anti-aircraft missile rocket engine nozzle (in Polish), *Military University of Technology Bulletin*, **LX**, 2, 47-61
11. SAFTA D., VASILE T., ION I., 2011, Regarding the influence of high frequency combustion instabilities on operation of solid rocket motors, *Problems of Mechatronics, Armament, Aviation, Safety Engineering*, **1**, 3, 7-24
12. SUTTON G.P., BIBLARZ O., 2001, *Rocket Propulsion Elements*, John Willey & Sons, Inc., New York
13. TORECKI S., 1984, *Rocket Motors* (in Polish), WKiŁ, Warsaw, pp. 260
14. WIŚNIEWSKI S., 1972, *Thermal Loads of Internal Combustion Engines* (in Polish), WKiŁ, Warsaw
15. WIŚNIEWSKI S., WIŚNIEWSKI T., 2000, *Heat Transfer* (in Polish), WNT, Warsaw
16. ŻYLUK A., PIETRASZEK M., 2014, Investigation of an additional oxidizer chage effect on selected characteristics of a solid-fuel rocket engine, *Journal of Theoretical and Applied Mechanics*, **52**, 1, 139-149

Manuscript received October 3, 2013; accepted for print March 4, 2014